Article

Assessing the Performance of Thin-Film Nanofiltration Membranes with Embedded Montmorillonites

Micah Belle Marie Yap Ang [1,*], **Amira Beatriz Gaces Deang [2]**, **Ruth R. Aquino [2]**, **Blessie A. Basilia [2,3]**, **Shu-Hsien Huang [1,4,*]**, **Kueir-Rarn Lee [1,*]** and **Juin-Yih Lai [1,5,6]**

[1] R&D Center for Membrane Technology and Department of Chemical Engineering, Chung Yuan Christian University, Taoyuan 32023, Taiwan; jylai@mail.ntust.edu.tw

[2] School of Chemical, Biological, and Materials Engineering and Sciences, Mapúa University, Manila 1002, Philippines; abgdeang@gmail.com (A.B.G.D.); rraquino@mapua.edu.ph (R.R.A.); basiliablessie@gmail.com (B.A.B.)

[3] Industrial Technology Development Institute, Department of Science and Technology, DOST Compound, Taguig City 1631, Philippines

[4] Department of Chemical and Materials Engineering, National Ilan University, Yilan 26047, Taiwan

[5] Applied Research Center for Thin-Film Metallic Glass, National Taiwan University of Science and Technology, Taipei 10607, Taiwan

[6] Graduate Institute of Applied Science and Technology, National Taiwan University of Science and Technology, Taipei 10607, Taiwan

* Correspondence: mbmyang@gmail.com (M.B.M.Y.A.); huangsh@niu.edu.tw (S.-H.H.); krlee@cycu.edu.tw (K.-R.L.)

check for updates

Abstract: In this study, the basal spacing of montmorillonite (MMT) was modified through ion exchange. Two kinds of MMT were used: sodium-modified MMT (Na-MMT) and organo-modified MMT (O-MMT). These two particles were incorporated separately into the thin-film nanocomposite polyamide membrane through the interfacial polymerization of piperazine and trimesoyl chloride in n-hexane. The membrane with O-MMT (TFN$_{O-MMT}$) has a more hydrophilic surface compared to that of membrane with Na-MMT (TFN$_{Na-MMT}$). When various types of MMT were dispersed in the n-hexane solution with trimesoyl chloride (TMC), O-MMT was well-dispersed than Na-MMT. The poor dispersion of Na-MMT in n-hexane led to the aggregation of Na-MMT on the surface of TFN$_{Na-MMT}$. TFN$_{O-MMT}$ displayed a uniform distribution of O-MMT on the surface, because O-MMT was well-dispersed in n-hexane. In comparison with the pristine and TFN$_{Na-MMT}$ membranes, TFN$_{O-MMT}$ delivered the highest pure water flux of 53.15 ± 3.30 L·m^{-2}·h^{-1} at 6 bar, while its salt rejection for divalent ions remained at 95%–99%. Furthermore, it had stable performance in wide operating condition, and it exhibited a magnificent antifouling property. Therefore, a suitable type of MMT could lead to high separation efficiency.

Keywords: montmorillonite; polyamide; thin-film nanocomposite; membrane separation; nanofiltration

1. Introduction

Treatment of industrial wastewater is vital before its discharge to rivers or soil land. The traditional treatment methods are screening, flotation, coagulation, and chlorination [1,2]. These methods are now at a disadvantage for consuming a lot of energy and requiring large working space to assemble. Conventional separation technique like membrane separation demonstrates its economical way of treatment [3,4]. One type of membrane separation is pressure-driven membrane filtration. Under this

process are the following methods: microfiltration, ultrafiltration, nanofiltration (NF), and reverse osmosis (RO). These processes are often combined, depending on the type of wastewater [5–7]. Among these, NF is widely used for its applicability to various industries, such as water purification and desalination [8,9], food and beverages [7,10,11], semiconductor [12,13], petroleum [14,15], pharmaceutical and biotechnology [16,17] and the textiles industry [18,19].

Several methods can be used to fabricate NF membranes. These are the phase-inversion process, polymer coating (dip coating, spin coating, or solution casting), layer-by-layer self-assembly, grafting, and interfacial polymerization [20,21]. Interfacial polymerization remains the preferred method, because the membranes formed during this process exhibited high permeability and selectivity. Furthermore, the polymerization reaction remains fast and easy to scale up compared to other methods. At present, there is a need to enhance the efficiency of the thin-film composite (TFC) membranes to cope with the fast-paced industrialization around the globe that results in an increase in the demand for clean water.

The membrane produced by interfacial polymerization is widely known as the thin-film composite (TFC) membrane. The TFC membrane is composed of a thin-film polyamide that forms on top of the polymer support. The reaction of interfacial polymerization occurs in two immiscible phases; commonly with water and organic solvent such as n-hexane, toluene, cyclohexane [22]. To increase the performance of the membranes, the following methods are used: modification of supporting layer [23,24], varying types of monomers [25,26], inclusion of another reactant in aqueous or organic phase [27,28], or the introduction of nanoparticles in the reaction [29,30]. Introducing inorganic nanoparticles enhances membrane performance and antifouling property without sacrificing salt rejections. With the rapid advancement of nanotechnology, researchers focus on developing nanoparticles to improve the TFC membranes. These nanoparticles are silica [29,31], silver [30,32], graphene or graphene oxide [33,34], zeolites [35,36], nanoclays [37–43], quantum dots [44,45], and carbon nanotubes [46,47]. TFC membranes with embedded nanoparticles are called thin-film nanocomposite (TFN) membranes [48,49]. Of all the nanoparticles, nanoclays are the most environmentally friendly and abundant. It is also preferable for its water purification capability, that can enhance the stability of the polymers in terms of structural, mechanical, and thermal [50,51]. Moreover, it requires a small amount of clay to boost the performance of the membrane [52].

Clays are naturally hydrophilic, which makes it favorable to embed in the polymer matrix with the improved wettability of the polymer. On top of this, they have a high adsorption capacity and surface area. They are small and exhibit a unique chemical composition with micro-porosity and a layered structure. They are divided into 5 different groups—kaolinite, montmorillonite (MMT), illite, and chlorite groups [53]. Among them, the MMT layers expand most, because their intermolecular spaces can be easily penetrated by water. In the year 1890, in the US, bentonite was discovered to contain MMTs [54]. Since then, bulk of MMTs are sourced from bentonite rocks. MMT has a 2-D layered structure, with each layer made of two silica tetrahedral sheets, with a central alumina octahedral sheet. The layers are intertwined oxygen atoms and exchangeable cations such as calcium, magnesium, sodium, and water molecules [55]. MMTs also have ions that may undergo ionic substitution, capable of producing useful new materials for various applications [53]. For the membrane applications, several scholars [37–43] attempted to embed different types of nanoclay in a polyamide matrix. Recently, Li et al. [37], modified a synthetic nanoclay–laponite by functionalizing it with different metal ions. They improved both the flux and antifouling properties of the polyamide membrane prepared using m-phenylenediamine (MPD), and trimesoyl chloride (TMC). Zhao et al. [38] used PEG 200 to assist in the dispersion of laptonite in an aqueous MPD solution. In their study, the flux of TFN membrane increased while maintaining NaCl rejection. Kadhom and Deng [39] prepared nano bentonite through the solvothermal method. At low bentonite concentration, there was an improvement in the flux and salt rejection of the RO membrane. Maalige et al. [40] incorporated a sulfonated bentonite in a polyamide membrane. Sulfonated bentonite altered the alignment of the polyamide chain; and enhanced the hydrophilicity and antifouling property of the membrane. Tajuddin et al. [41,42] used an

anionic clay-layered double hydroxide in fabricating the NF membrane from the reaction of piperazine (PIP) and TMC. They also improved both water flux and the antifouling property of the membrane. Dong et al. [43] compared the influence of anionic and cationic clays when embedded in polyamide membranes. The anionic clay was represented by a double layered hydroxide, while the cationic clay was represented by MMT. The particles were dispersed in a TMC solution. Both particles changed the property of the RO membranes. On the other hand, the membrane with MMT showed higher RO performance than that of the membrane with double layered hydroxide nanoparticles.

The majority of the studies embedded the clay in the polyamide membrane made of MPD and TMC monomer for RO. In NF, PIP is the commonly used monomer. Polyamide made from PIP and TMC do not possess the same membrane properties with a polyamide prepared from MPD and TMC. Because MPD has primary amines and benzene group, whereas PIP has secondary amines and no benzene group, they produce different cross-linking degree when they react with TMC. Our study aimed to improve the separation efficiency of the NF membrane using two modified MMT and compare their effect with the property of the TFN membrane. These two types of MMT particles were sodium- and surfactant- intercalated MMT. Adding MMT to the polyamide layer creates a water pathway made from the interface between MMT and polyamide. These water pathways improved the separation efficiency. Its dispersion in different solvents is easy to control through the functionalization of monomers by ion exchange. Furthermore, because MMT is abundant in the environment, it also reduces the preparation cost of the TFN membranes. Following our previous work [29], that showed the economical side of putting the particles in an organic phase, the MMTs were dispersed in TMC in a n-hexane solution. The two MMTs exhibited different dispersion properties depending on the element or compound that is intercalated in the nanosheet of the MMT. This factor was studied through membrane characterization and a performance test.

2. Materials and Methods

2.1. Materials

Philippine MMT was provided by Material Science Division, Industrial Technology Development Institute of the Department of Science and Technology, Taguig City, Philippines. Its property was similar to the previous work [56]. Sodium carbonate, manufactured by Ajax Chemicals Ltd., Sydney, Australia, was used to improve the basal spacing of Philippine MMT. Dialkyldimethyl ammonium chloride (DDAC) was a product of Hoechst Altiengesellschaft, Frankfurt, Federal Republic of Germany. Polysulfone (PSf) pellets (UDEL P-3500) and a nonwoven polyester, as a raw material for the support layer, were obtained from Amoco Performance Product, Ridgefield, CT, USA, Ahlstrom, Helsinki, Finland, respectively. N-methyl-2-pyrrolidone (NMP), as a solvent of PSf, was acquired from Tedia Company, Inc. (Fairfield, OH, USA). Polyethylene glycol (PEG) 20k (as additive ng PSf support) and PIP (as diamine monomer) were purchased from Alfa Aesar (Heysham, Lacashire, England). TMC (as an organic monomer) was supplied by Tokyo Chemical Industry Co. Ltd. (Tokyo, Japan). n-Hexane was from Echo Chemical Co. Ltd. (Miaoli, Taiwan). Bovine serum albumin (BSA) and phosphate buffer saline were procured at UniRegion Bio-Tech (USA). The following solutes were bought from Sigma-Aldrich (Saint Louis, MO, USA): Na_2SO_4, $MgCl_2$, $MgSO_4$, and NaCl. Distilled water was produced in the laboratory using the Lotun ultrapure water system (Lotun Technic Co. Ltd., New Taipei, Taiwan).

2.2. Synthesis of Philippine Sodium-montmorillonite and Organo-montmorillonite

In a beaker, 100 g of MMTs was dehydrated at 100 °C. Afterwards, it was mixed with 1000 mL water and 3 g of sodium carbonate to form a paste texture. The paste was mixed for 30-min at room temperature. Once dehydrated, the MMTs were pulverized for 15 min. Then, 375 mL of water was added to form the mixture into a paste for the second time. Lastly, it was dried at 100 °C and pulverized using a mechanical grinder. MMTs were sieved with a 200-mesh. The particles that passed through

200-mesh were used in the study. The cationic exchange capacity of Na-MMT is 84.2, which is according to the BaCl$_2$/MgSO$_4$ method [57].

The functionalization of the organic material on Na-MMT was based on the work of Favre and Lagaly [58]. DDAC was used as organic material to modify the MMTs. The amount of DDAC was 1.5 times of CEC of Na-MMT. On one blunger, 100 g of Na-MMT was mixed with DDAC for 30 min and it was transferred to a stoppered glass container to react with DDAC and Na-MMT for 72-h at 70 °C. Then, it was washed several times until the amount of C and N in the particles were constant, which was determined by a CNS-2000 Elemental Analyzer (LECO Corporation, Minneapolis, MN, USA). The obtained organically modified MMTs were called organo-modified MMT (O-MMT). MMTs were dried at 80 °C, then were pulverized, and were sieved with a 200-mesh. Afterwards, they were dried again at 70 °C for 24-h and were then transferred to a vacuum desiccator.

2.3. Preparation of Thin-film Nanocomposite Membranes

The PSf support was similar to our previous work [59]. Inside a mechanical mixer, a 16 wt % PSf/NMP solution with a total volume of 4 L was dissolved for 24-h. Then, it was transferred to a 5 L bottle and kept in the oven at 30 °C. After 24-h of degassing, the PSf solution was poured into a continuous casting machine that was equipped with a non-woven polyester—PSf was precipitated on top of the non-woven. This PSf support was transferred to a water bath and washed for a day, before it was stored in 1 wt % sodium bisulfite.

Figure 1 illustrates the preparation of the TFN membranes. Two types of MMTs were dispersed in the n-hexane solution of TMC. The material that was intercalated in the MMT affects the behavior of the clay in the oil solution [60]. Intercalating DDA$^+$ to MMT would result in a better dispersion of MMT in the n-hexane solution than intercalating Na$^+$. In Figure S1 (Supplementary Materials) are the photographs of the Na-MMT and O-MMT in n-hexane. The amount of the particle was fixed at 0.05 g O-MMT/50 mL n-hexane (low concentration) and 0.5 g of MMT/15 mL n-hexane (high concentration). Dispersing MMTs at low concentration cannot differentiate. On the other hand, at high concentration, Na-MMT settles immediately for less than 30 s, whereas O-MMT was still well-dispersed.
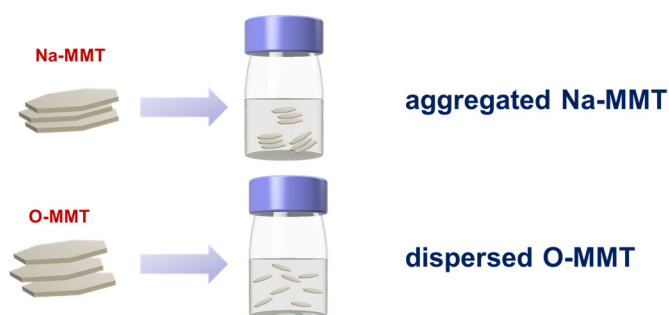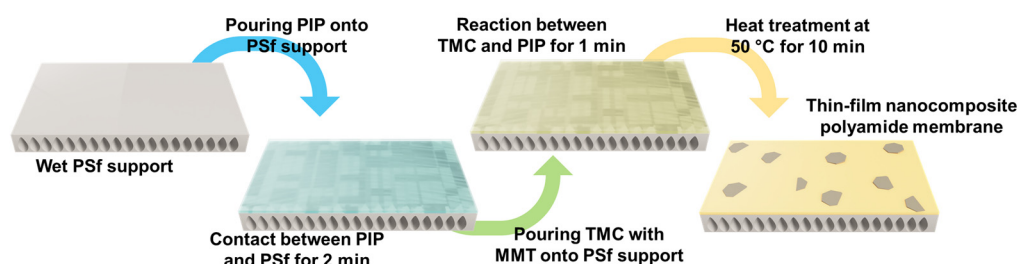

Figure 1. Schematic diagram of membrane preparation.

In the next step, 361 cm^2 of PSf support was cut and washed three times with distilled water. Then, it was clamped to a metal holder and followed by pouring a 0.35 wt % aqueous PIP solution on the membrane surface. After 2 min, the solution was removed and disposed of in a waste bottle. The excess droplets on the surface were removed using an airgun at a pressure of 1 bar. Afterwards, the saturated membrane of PIP was again clamped on a metal plate. Then, 0.2 wt % TMC in n-hexane was poured on the PSf surface, and after a contact with the TMC solution, a thin-film polyamide layer formed in 1 min. The membrane was heat-treated at 50 °C for 10 min, then washed three times using distilled water. For the membranes containing MMT, 0.05 to 0.75 g of MMTs/g of TMC were added to a TMC in the n-hexane solution.

The membrane without MMTs was represented as TFC, whereas the membranes with MMTs were denoted as TFN$_X$, where X stands for the Na-MMT or O-MMT.

2.4. Characterization of Montmorillonites and Composite Membranes

Attenuated total reflectance-Fourier transform infrared (ATR-FTIR) spectroscopy (Perkin Elmer Spectrum 100 FTIR Spectrometer, Waltham, MA, USA) was utilized to compare the chemical structure of MMTs and membranes. X-ray photoelectron spectroscopy (XPS, VG K-alpha ThermoFisher Scientific, Inc. Waltham, MA USA) determined the elemental composition of the membrane surface. Field emission scanning electron microscopy (FESEM, S-4800, Hitachi Co, Tokyo, Japan) was used to take the morphology of MMT and the membranes. The FESEM installed with energy dispersive X-Ray spectroscopy (EDX, Ultim$^®$ Max, Oxford Instruments, High Wycombe, UK) obtained the Na content on the surface of the membrane. The surface roughness of the membranes was examined by an atomic force microscopy (AFM, NanoScope$^®$ V, Bruker, Billerica, MA, USA). The MMTs were observed using transmission electron microscopy (TEM, JEOL JEM-2100, Tokyo, Japan). Thermodynamic gravimetric analysis (TGA, Q500, TA Instrument, USA) was employed to verify the degradation temperature of the MMTs. The crystallinity of the MMT and membranes were determined with X-ray diffraction (XRD, Model D8 Advance Eco, Bruker, Billerica, MA, USA). The charges of the MMTs were acquired using a dynamic light scattering instrument (DLS, Zeta Nano ZS, Malvern, UK), whereas the surface charge of the membrane was measured by a SurPASS Electrokinetic Analyzer (Anton Paar, New South Wales, Australia) under pH 3, 7, and 11. The membrane hydrophilicity was determined through an automatic interfacial tensiometer (PD-VP Model, Kyowa Interface Science Co. Ltd., Niiza-City, Saitama, Japan), with water droplet size of 5 µL during testing.

2.5. Evaluation of Nanofiltration Performance

Simultaneously, 4 pieces of membranes were tested in a crossflow device. Each membrane cell has an effective area (A) of 12.57 cm^2. The membrane underwent a precompression at 6.5 bar for 1-h. After that, the pure water flux (J) was measured at 6 bar. The flux and salt rejection (R) were evaluated through the following equations:

$$J = \frac{m}{\rho A t} \tag{1}$$

$$R = \frac{C_f - C_i}{C_f} \times 100\% \tag{2}$$

where *m* (kg) was the mass of permeate collected at time t (h), ρ was the water density (1 kg/L), and C_f and C_i were the concentrations of salt in feed (1000 ppm) and permeate, respectively. The salt concentration was measured using a Mettler Toledo SevenMulti (Schwerzenbach, Switzerland).

2.6. Evaluation of Antifouling Property and Stability of the Membrane

A crossflow filtration setup was used to evaluate the antifouling property of the membranes. The membrane was pre-pressurized at 6.5 bar for 1-h through supplying a distilled water. After 1-h, the pressure was decreased to 6 bar and the flux was measured every 10 min. (1) The feed was then

replaced with a solution containing 0.1 g/L BSA, and 1000 ppm aqueous Na_2SO_4 solution. The pH was maintained at 7.4, through the addition of phosphate buffered saline solution. (2) The flux was measured every 10 min for 1-h. (3) Afterwards, this was washed by supplying distilled water for 15 min at 1 bar and another 15 min at 6 bar. (4) Then, the feed was swapped with fresh distilled water and the flux was measured three times every 10 min. Procedures (1) to (4) were repeated twice.

For the stability test, the membrane was precompressed for 1-h at 6.5 bar with distilled water. The feed was replaced with 1000 ppm Na_2SO_4, then flux and rejection were obtained at 6 bar. The operation was continued for 169-h. Flux and salt rejection were determined at random times.

3. Results and Discussion

3.1. Characterization of Montmorillonite

Figure 2a indicates the ATR-FTIR of Na-MMT and O-MMT particles. The Na-MMT and the O-MMT had a peak at 3620 and 3675 cm^{-1}, respectively. These peaks correspond to hydroxyl groups of MMT. However, only Na-MMT had a peak at 3415 cm^{-1}, which was attributed to its bound water molecules. For O-MMT, the peak of water molecules cannot be observed because of the intercalation of DDA^+ on the interlayer spaces of MMT. When Na-MMT and DDAC underwent an ion exchange, DDA^+ replaced the Na^+. The hydrophobic alkanes chains of DDA^+ cannot catch water molecules. The Si-O-Si of the Na-MMT and O-MMT was located at 990 and 1031 cm^{-1}, whereas the stretching vibration of Al-O-(OH)-Al was at 910 cm^{-1}. The H-OH bond from water molecules that was retained in the MMT was positioned at 1635 cm^{-1}. Carbonates in the MMT were located at 1460 cm^{-1}. New peaks were appeared from O-MMT at 2850 and 2915 cm^{-1}, which ascribed to the -CH_2 and -CH_3 stretching vibration of long alkyl chain of DDA^+, respectively. Moreover, the peak at 2988 cm^{-1} was corresponded to the N-H stretching of amine salts [61–64].

The degradation temperature and percent residue of MMT were determined using thermogravimetric analysis (Figure 2b). The Na-MMT reduced its weight by 0.16% within the temperature range of 50 and 100 °C—this loss was from the adsorbed water. Between the temperature of 100—700 °C, 6.91% was lost because of the dehydroxylated of aluminosilicate layer. Hence, the total weight loss of Na-MMT was 7.04%. On the other hand, O-MMT had a total weight loss of 46.43%. The larger difference in weight loss of O-MMT than Na-MMT was because of the presence of the DDA^+. Ahmad et al. [65] reported similar results. At 50 to 100°C, the O-MMT lost the bound water. Two elements decomposed between the temperature range of 100 and 700 °C; these were the amine salts of DDA^+ and the dihydroxylation of aluminosilicate layer.

Figure 2c,d confirms the intercalation of Na^+ and DDA^+ in MMT. Inglethorpe et al. [57] obtained similar results; that the basal spacing of Na-MMT was 12.65 Å, under normal relative humidity. After swelling the Na-MMT in n-hexane solution, the d-spacing increased to 12.81 Å. Thus, Na-MMT was swollen by the n-hexane only. When some Na^+ was replaced with DDA^+, at 2Θ range from 2°–10°, three basal spacing emerged. These spacings had values of 37.12, 18.07 and 12.01 Å, indicating that the O-MMT was composed of paraffinic, mono-, and bi-layers, respectively [66,67]. Therefore, O-MMT had Na^+ and DDA^+ that was intercalated in the MMT nanosheets. When O-MMT was dispersed in n-hexane, the d-spacing enlarged at a greater degree. Spaces of the bilayers increased from 12.01 to 12.94 Å; monolayers transformed to pseudotrimolecular layers from 18.07 to 19.68 Å; and paraffinic layers also expanded from 37.12 to 39.09 Å. Figure 2e defines the zeta potential of the particles at pH 7. Na-MMT had a negatively charged surface of −24.07 ± 3.53 mV, because it is composed of an aluminosilicate that emits electronegativity. However, after intercalation of DDA^+, the net charge of O-MMT particles became −7.60 ± 1.92 mV. This was because the DDA^+ neutralized some part of the aluminosilicate. Therefore, intercalating DDA^+ changed the net charge of MMTs into less negatively charged MMTs [68,69].

Figure 3 reveals the TEM images of Na-MMT and O-MMT nanoparticles. The random stacking of MMT was visible. The distance between sheets was difficult to measure, because MMT consists of

sheets that were folded at the edges. Table S1 (Supplementary Materials) enumerates the surface area, pore volume and pore size of the MMTs. Na-MMT and O-MMT had Brunauer–Emmett–Teller surface areas of 40.12 and 5.05 $m^2 \cdot g^{-1}$, respectively. The pore size of Na-MMT was 129.23 Å, whereas O-MMT was 205.34 Å.
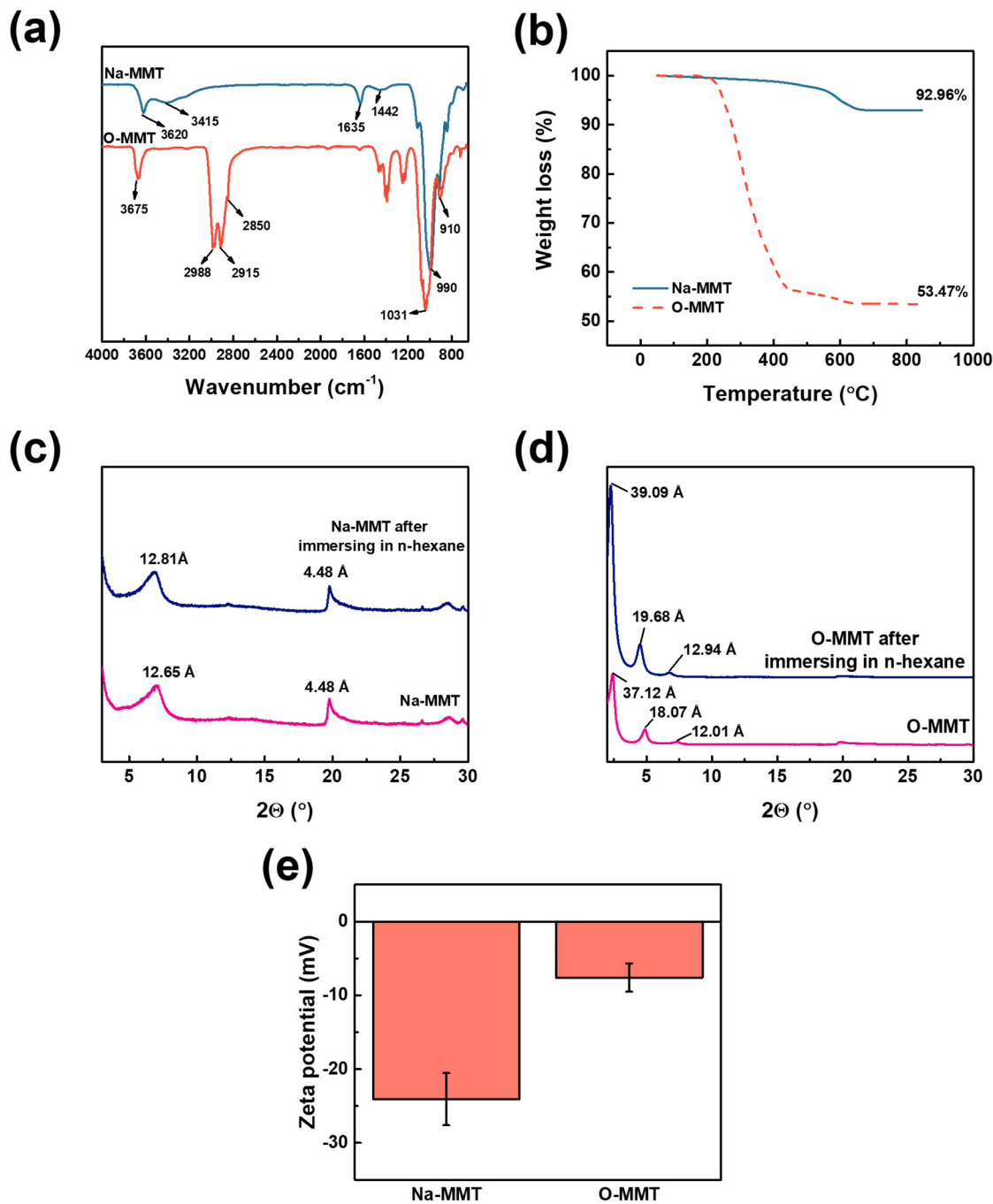
Figure 2. (**a**) ATR-FTIR spectra; (**b**) thermogravimetric analysis; (**c**,**d**) crystallinity; (**e**) zeta potential of the Na-MMT and organo-modified MMT (O-MMT).
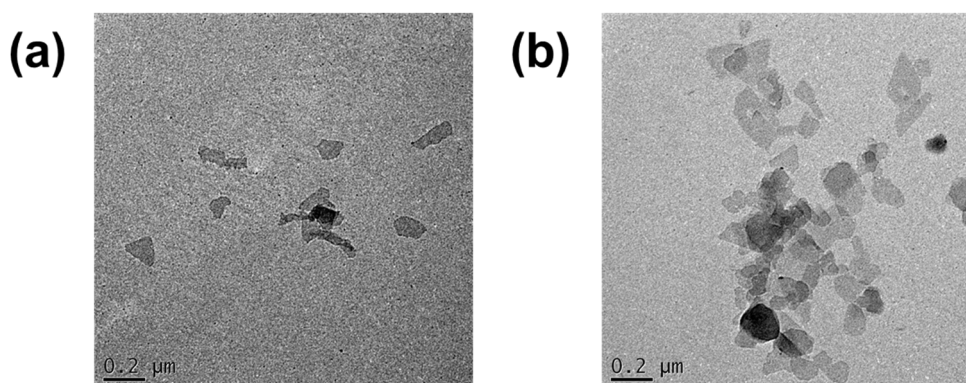
Figure 3. Particle morphology of (**a**) Na-MMT and (**b**) O-MMT.

3.2. Characterization of the Membranes

3.2.1. Surface Chemical Composition

Figure 4 indicates the chemical structure of PSf support, TFC, and TFN membranes. The peaks at 1587, 1504, and 1488 cm^{-1} were attributed to the aromatic rings of PSf support. The asymmetric and symmetric S = O stretching vibrations of PSf were located at 1327–1293 and 1178–1147 cm^{-1}, respectively [70,71]. The PSf support had a peak at 3360 cm^{-1}, which was attributed to the addition of PEG 20k into the PSf solution [72]. TFC and TFN membranes also had a broad peak at 3100–3650 cm^{-1}, corresponding to O-H and N-H stretching of the carboxylic acid and secondary amine, respectively. The carboxylic acid was from the hydrolysis of TMC, formed during the washing of the membrane using water. The secondary amine was from the PIP monomer that was not reacted with the acyl chloride of TMC. A new peak was found at 1620 cm^{-1} for TFC and TFN membranes, assigned to the amide I of polyamide layer formed from the reaction of PIP and TMC [73–75]. The peak of MMT, however, cannot be seen, because of the overlapping spectra of PSf support and MMT. It was also possible that particles on the sample were too few to be detected. Therefore, XPS (Table 1) and EDX (Figure 5) scanned the elemental composition on the membrane surface.
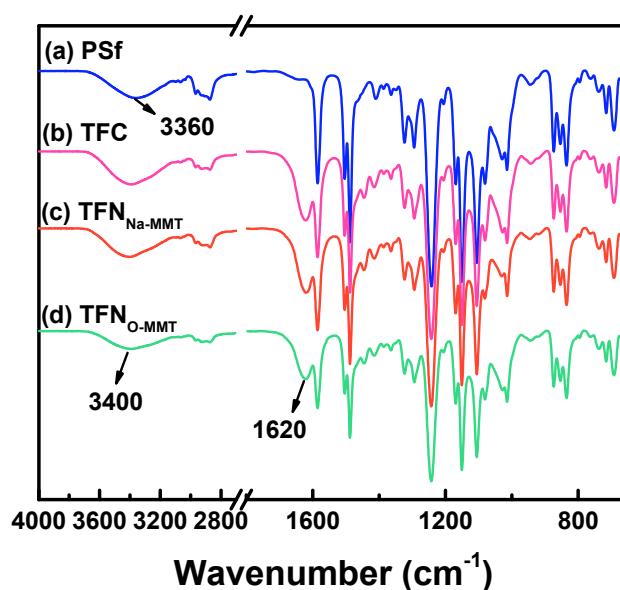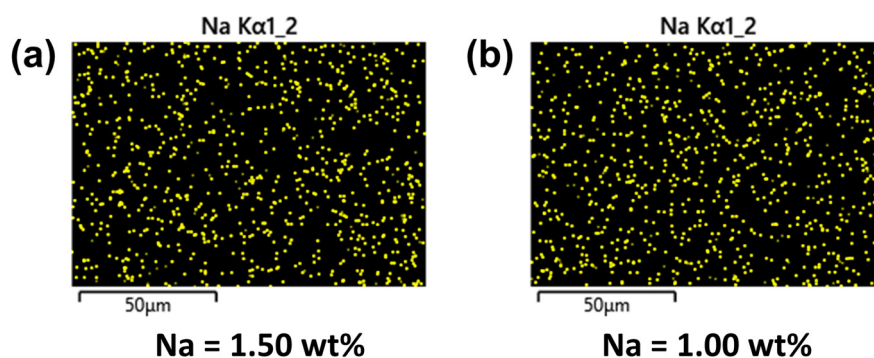

Figure 4. ATR-FTIR spectra of polysulfone (PSf), thin-film composite (TFC) and thin-film nanocomposite (TFN) membranes. Particle concentration = 0.05 g O-MMT/g TMC.

Table 1. Elemental composition of the membrane surface from XPS analysis.

|	C (%)	O (%)	N (%)	Other Elements (%) [a]
TFC	70.3	16.9	12.9	
TFN$_{Na-MMT}$	74.8	14.5	7.64	3.02
TFN$_{O-MMT}$	71.3	16.6	8.69	3.38

[a] Ca, Na, Si, Fe, Al, Mg, Ti, P, K.

Figure 5. EDX mapping of Na element: (**a**) TFN$_{Na-MMT}$; (**b**) TFN$_{O-MMT}$. Particle concentration = 0.05 g O-MMT/g trimesoyl chloride (TMC).

Table 1 lists the elemental composition of TFC and TFN membranes. The TFC membrane only contained 70.3% C, 16.9% O and 12.9% N. By incorporating MMT into the polyamide layer, new elements were detected, such as Ca, Na, Si, Fe, Al, Mg, Ti, P, and K. These elements were common for MMT. TFN$_{O-MMT}$ had higher N content than that of TFN$_{Na-MMT}$, because the amine salt DDA$^+$ was intercalated into O-MMT of TFN$_{O-MMT}$. Figure 5 mapped the dispersion of the Na element on the TFN membrane surface, using EDX analysis. Because MMT also contains some Na$_2$O on the nanosheet [76], it was used to monitor the dispersion of MMT on the membrane surface. Other elements could have been blocked by the X-ray in the EDX. Both TFN membranes showed a uniform distribution of the Na element of MMT. TFN$_{Na-MMT}$ had more Na (1.5 wt %) on the surface, because the particle embedded here was modified by Na$^+$. TFN$_{O-MMT}$ had only 1.0 wt % Na, because Na$^+$ of Na-MMT was replaced by the DDA$^+$ of the surfactant. Therefore, the Na on the surface of TFN$_{O-MMT}$ could be from the Na$_2$O of the MMT and some Na$^+$ that was not replaced by DDA$^+$.

3.2.2. Membrane Morphology and Structure

Figure 6 presents the surface FESEM images of PSf support, TFC, and TFN membranes. The TFC membranes had nodules on the surface, which was a typical surface for a polyamide membrane prepared from PIP and TMC. When Na-MMT was embedded, the TFN$_{Na-MMT}$ had a less uniform surface and the aggregation of Na-MMT on the surface was visible. The aggregation of Na-MMT on the polyamide surface was the result of poor dispersion of Na-MMT nanosheets in n-hexane. When Na-MMT was immersed with an oil solution, only a swelling of the nanosheet in the oil would occur [60]. This could result to numerous lamellar stackings of Na-MMT on the polyamide matrix. To improve the property of MMT, Na-MMT was modified through ion exchange using DDAC. DDAC is a surfactant with a hydrophobic tail and a hydrophilic head that would help the MMT to disperse better in the n-hexane solution. Compared to TFN$_{Na-MMT}$, TFN$_{O-MMT}$ had less aggregation of O-MMT on the surface, because O-MMT dispersed well in in-hexane solution. Thus, O-MMT distributed more uniformly into the polyamide structure after interfacial polymerization compared to Na-MMT nanoparticles.
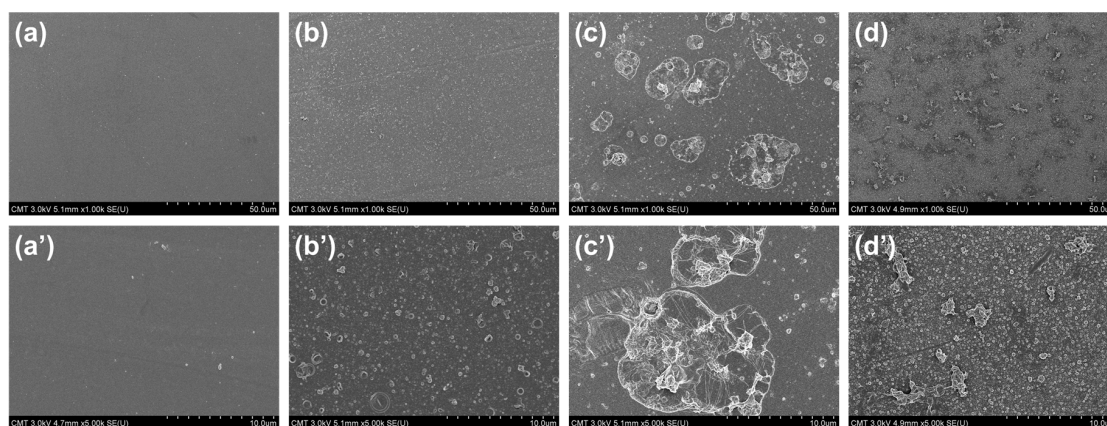
Figure 6. Surface field emission scanning electron microscopy (FESEM) images (magnification = ×1k and ×5k) of (**a**,**a'**) PSf, (**b**,**b'**) TFC, (**c**,**c'**) TFN$_{Na-MMT}$ and (**d**,**d'**) TFN$_{O-MMT}$. Particle concentration = 0.05 g O-MMT/g TMC.

The surface roughness also affected the membrane performance (Figure 7). AFM analysis had similar results with surface FESEM images (Figure 6) of the membranes. PSf support had the smoothest surface with a root mean square (Rq) of 4.61 ± 0.69 nm. When PIP and TMC reacted on top of the PSf to form a polyamide layer, the surface roughness increased to 11.08 ± 2.15 nm. This increase in surface roughness was because of the nodules on its surface (Figure 6b). Compared to TFN$_{O-MMT}$ (42.1 ± 1.94 nm), TFN$_{Na-MMT}$ had a higher surface roughness (51.96 ± 23.89 nm). This high surface roughness was from the aggregation of the Na-MMT on the polyamide matrix. The O-MMT was well-dispersed when transferred to the n-hexane solution compared to the Na-MMT, thus, the lamellar nanosheets of Na-MMT had a higher tendency to aggregate when embedded on polyamide layer. Nevertheless, both TFN membranes had a higher surface roughness than that of TFC. The advantage of a membrane with rougher surface is that there is a larger area for water to contact, therefore providing higher water flux. Similar to other works [42,77,78], embedding nanoparticles enhanced the surface roughness of the polyamide.
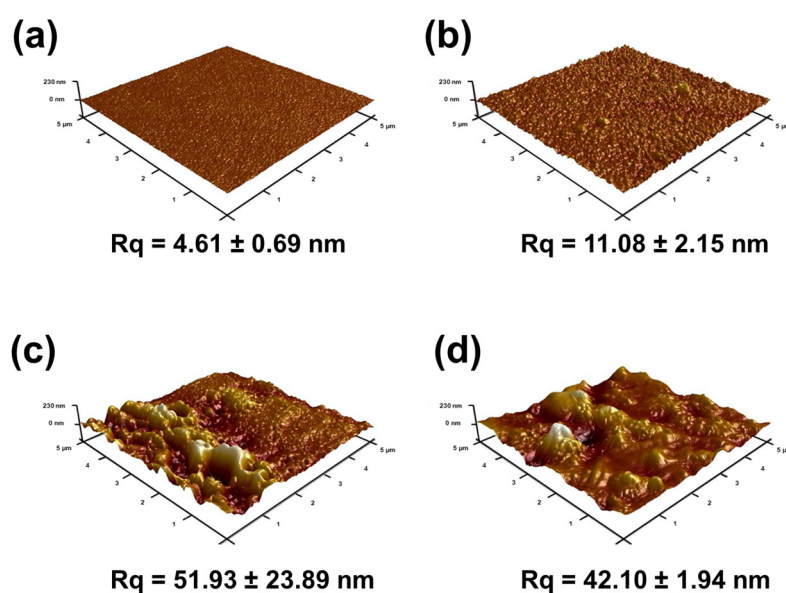
Figure 7. Three-dimensional atomic force microscopy (AFM) images of (**a**) PSf, (**b**) TFC, (**c**) TFN$_{Na-MMT}$ and (**d**) TFN$_{O-MMT}$. Particle concentration = 0.05 g O-MMT/g TMC.

The thickness of the polyamide layer may be observed through the photo of cross-sectional FESEM images (Figure 8). When the polyamide layer was deposited on PSf surface, a thin layer of polyamide was formed, with an average thickness of about 116.11 ± 10.56 nm. However, incorporating either Na-MMT or O-MMT, TFN membrane had a thinner polyamide layer than that of TFC membrane, which was approximately 113 nm. The decrease in thickness of the polyamide may have transpired during interfacial polymerization, when MMT possibly prevented some TMC to react with PIP, therefore slowing down the reaction rate. Other works [59,77] also obtained similar findings.
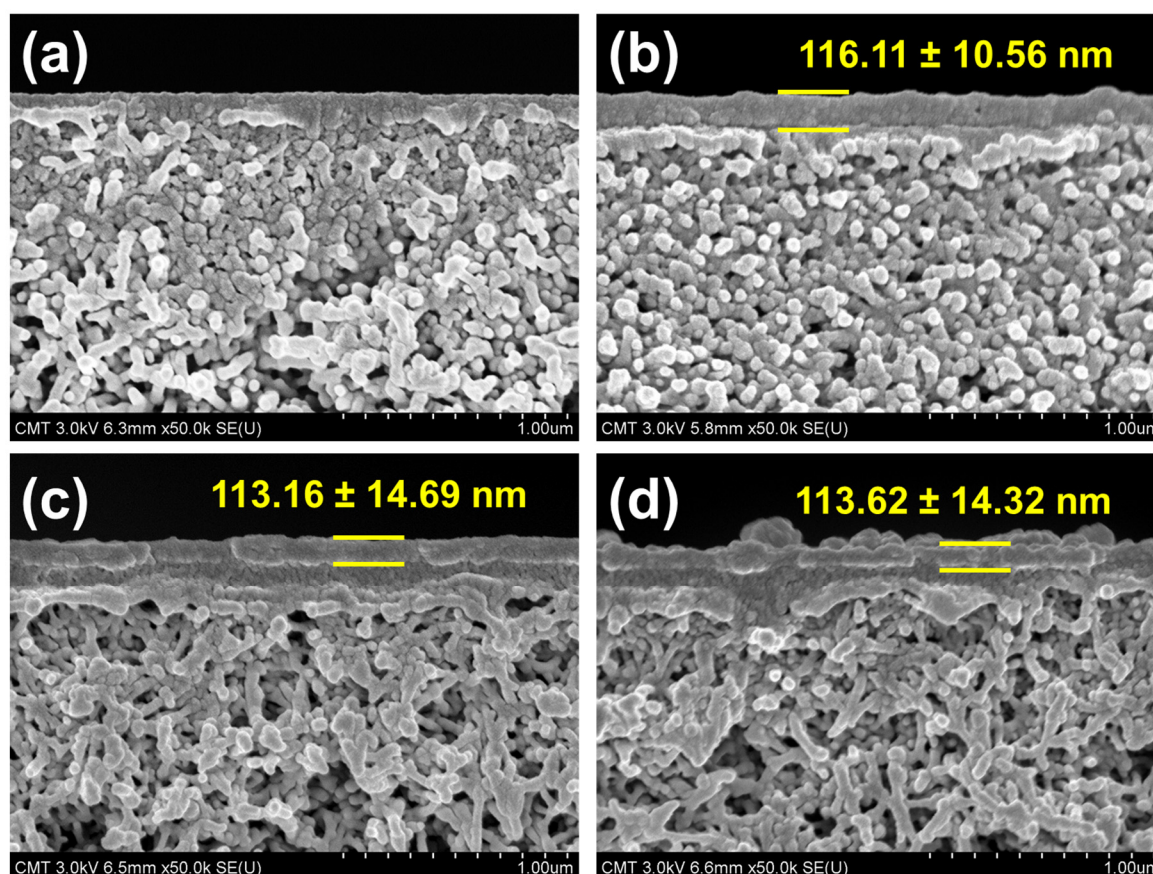
Figure 8. Cross-sectional FESEM images of (**a**) PSf, (**b**) TFC, (**c**) TFN$_{Na-MMT}$ and (**d**) TFN$_{O-MMT}$. Particle concentration = 0.05 g O-MMT/g TMC.

3.2.3. Crystallinity, Wettability and Surface Charge

Figure 9a evaluates the crystallinity of the membrane. However, there was no difference on the XRD patterns of PSf, TFC, and TFN membranes. All the peaks were corresponded to the spectra of PSf support. Furthermore, no peaks of Na-MMT or O-MMT were observed on TFN membranes—indicating that the particles on the polyamide were exfoliated. The water contact angle of the membranes defines their hydrophilicity. Two factors can affect the water contact angle—the surface functional groups and the surface roughness. Figure 9b reveals that TFN$_{O-MMT}$ had the lowest water contact angle, because of the hydrophilic nature of O-MMT. In addition, TFN$_{O-MMT}$ had a rougher surface (Figure 7) than that of TFC, therefore providing a larger area for water to contact [79]. The water contact angle of the membranes was as follows: PSf = 58.98 ± 2.88°; TFC = 33.23 ± 2.96°; TFN$_{Na-MMT}$ = 31.95 ± 2.59°; TFN$_{O-MMT}$ = 21.69 ± 2.79°.
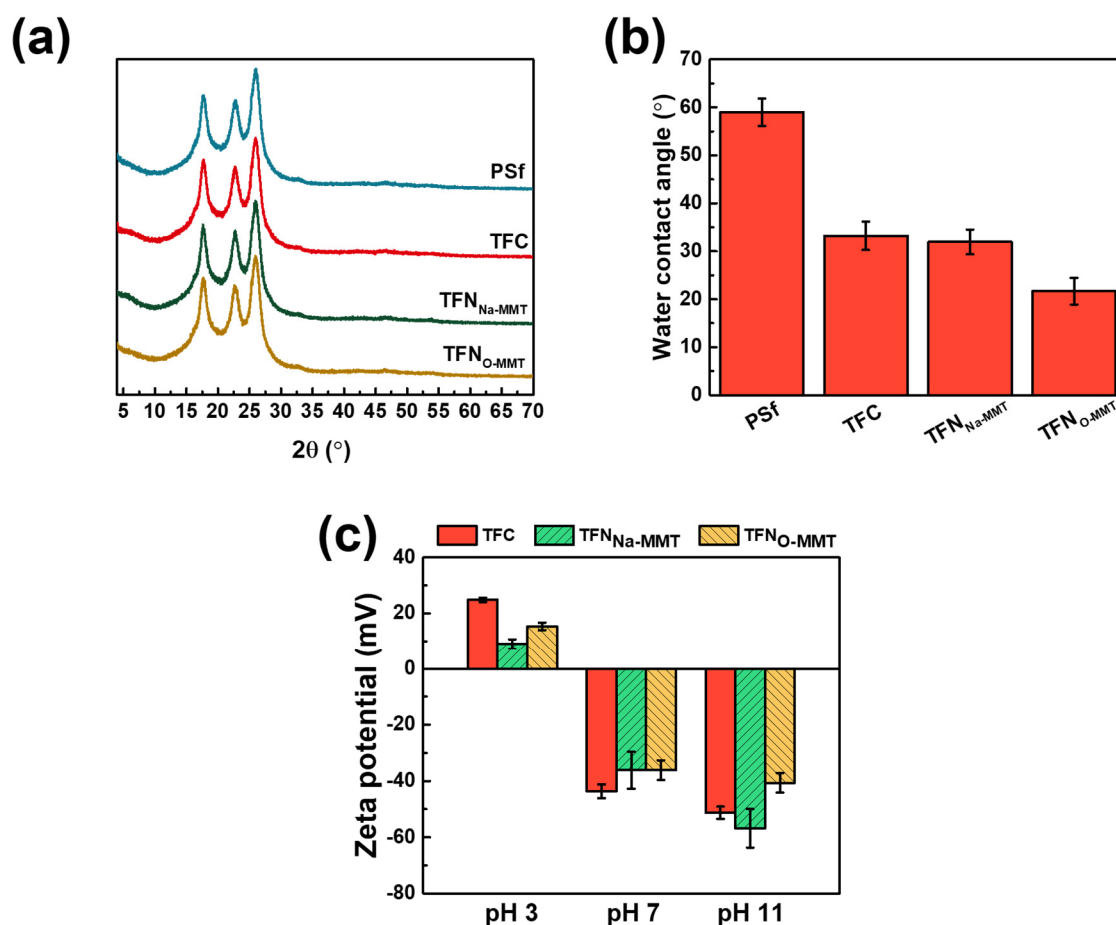
Figure 9. (**a**) XRD analysis; (**b**) water contact angle; and (**c**) zeta potential analysis of the membranes. Particle concentration = 0.05 g O-MMT/g TMC.

Figure 9c evaluates the surface zeta potential of the TFC and TFN membranes at pH 3, 7, and 11. At pH 3, all membranes had a positively charged surface, because their amine group protonated to NH^+ thus giving a surface with net positive charge. The order from high to low of the zeta potentials at pH 3 were as follows: TFC (24.86 ± 0.78 mV) > TFN$_{O-MMT}$ (15.30 ± 1.34 mV) > TFN$_{Na-MMT}$ (8.94 ± 1.75 mV). During interfacial polymerization of the TFC membrane, no particle hindered the reaction of PIP and TMC, thus producing more amide groups on the membrane surface and less carboxylic acid group from the hydrolysis of TMC, resulting in a more positively charged surface. TFN$_{O-MMT}$ had a more positively charged surface than that of TFN$_{Na-MMT}$ at pH 3. Because TFN$_{O-MMT}$ had DDA$^+$ intercalated in O-MMT lamellar sheets, its amine salt also protonated, probably producing a more positively charged membrane than that of TFN$_{Na-MMT}$. At pH 7 and 11, all membranes had a negatively charged surface. For the TFC membrane, only carboxylic acid groups deprotonated to COO$^-$, whereas TFN membranes had aluminosilicates that also deprotonated. Therefore, TFN$_{Na-MMT}$ and TFN$_{O-MMT}$ had similar zeta potential of -36 mV, whereas TFC had -43 mV. The net charge of TFC membrane at pH 7 was more negative, because there was no particle on its surface that would contribute positively charged molecules. However, TFN$_{Na-MMT}$ exhibited the most negative at a very basic condition (pH 11), because Na-MMT was abundant with an aluminosilicate that also deprotonates. For TFN$_{O-MMT}$, it had DDA$^+$ that was intercalated in the O-MMT—produces less negative on the net charge of the membrane at pH 11. Nevertheless, the zeta potential of the membranes at pH 3 to 11 was similar to a negatively charged NF membrane.
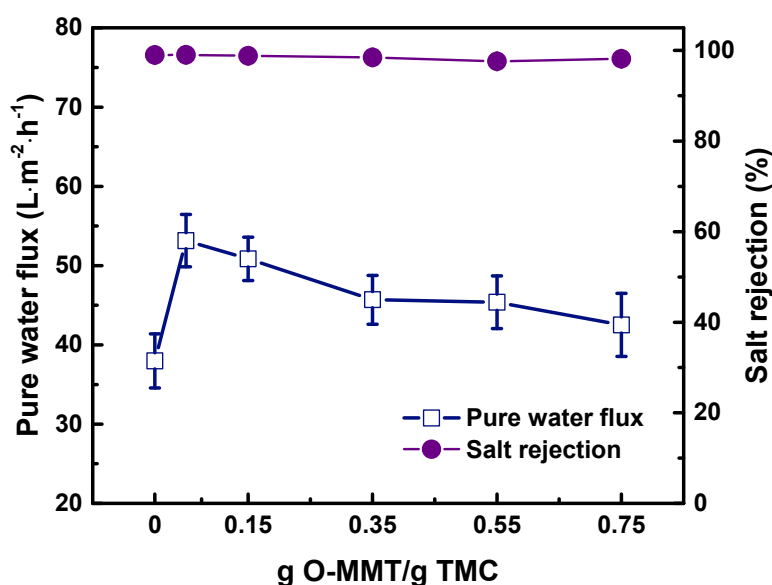
3.3. Nanofiltration Performance

Figure 10 compares the performance of TFC and TFN membranes using four different salts. TFN$_{\text{O-MMT}}$ had the highest pure water flux of 53.15 ± 3.30 L·m^{-2}·h^{-1}because it had the most hydrophilic surface. Compared to the TFC membrane (37.98 ± 3.41 L·m^{-2}·h^{-1}), TFN$_{\text{Na-MMT}}$ had a higher pure water flux (41.24 ± 3.53 L·m^{-2}·h^{-1}), because it had a rougher surface, where more water could contact on its surface, resulting in a higher flux. The salt rejection of all membranes follows the typically negatively charged membranes: Na$_2$SO$_4 \cong$ MgSO$_4 >$ MgCl$_2 \cong$ NaCl. The ions had the following hydrated radii in decreasing order: Mg^{2+} (0.43 nm) $>$ SO$_4{}^{2-}$ (0.38 nm) $>$ Na$^+$ (0.36 nm) $>$ Cl$^-$ (0.33 nm) [80]. The rejection for Na$_2$SO$_4$ and MgSO$_4$ of all membranes was approximately between 95% and 99%. Na$_2$SO$_4$ and MgSO$_4$ contain divalent anions. According to Donnan exclusion theory [81], a negatively charged membrane surface rejects divalent anions efficiently. However, after incorporating Na-MMT or O-MMT on the membrane, the MgCl$_2$ and NaCl rejection of TFN membrane became relatively lower than that of TFC membrane. Because during interfacial polymerization, MMT interfered in the reaction of PIP and TMC, resulting in a less cross-linked structure of the polyamide. In addition, Na$^+$ and Cl$^-$ have a weaker electrical charge and a smaller hydrated radius compared with divalent ions. Thus, the rejection of NaCl for TFN membranes was lower than that of TFC. Nonetheless, the TFN$_{\text{O-MMT}}$ membrane had a higher selectivity on the divalent salts over the monovalent salts.
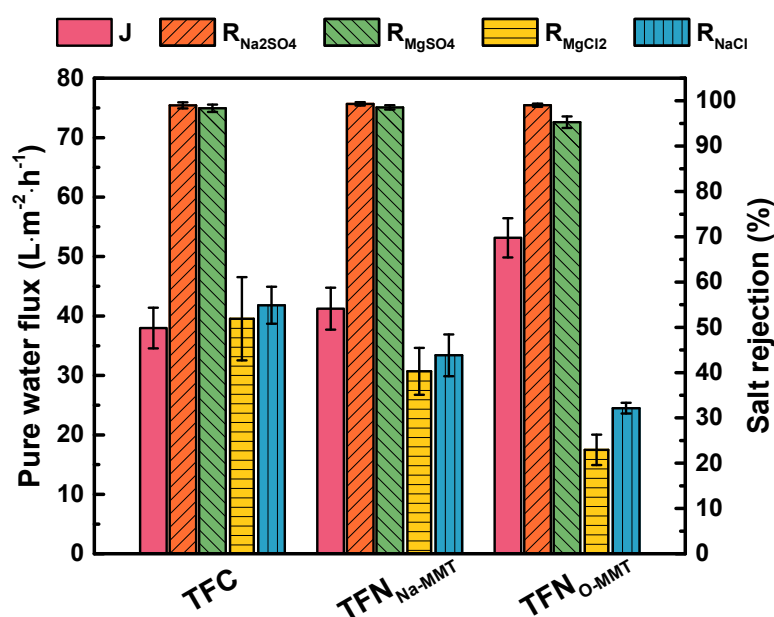
Figure 10. Nanofiltration performance of composite membranes. Feed = 1000 ppm salt solution; Operating condition: pH = 7, 6 bar, 30 °C. Particle concentration = 0.05 g O-MMT/g TMC.

Figure 11 plots the amount of O-MMT vs. NF performance. At 0.05 g O-MMT/g TMC, the TFN$_{\text{O-MMT}}$ delivered the highest performance: pure water flux = 53.15 ± 3.30 L·m^{-2}·h^{-1}; rejection of Na$_2$SO$_4$ = $99.04 \pm 0.35\%$. However, at above 0.05 g O-MMT/g TMC, the pure water flux began to decrease. This was because at a high concentration of O-MMT, it still act as a barrier for water to pass through, leading to an increase in mass transfer resistance and led to low water flux. Therefore, when the amount of O-MMT was increased from 0.05 to 0.75 g O-MMT/g TMC, the pure water flux simultaneously decreased from 53.15 ± 3.30 to 42.51 ± 3.98 L·m^{-2}·h^{-1}. Nevertheless, there was an improvement in membrane performance at the optimum concentration of O-MMT.

Figure 11. Nanofiltration performance of TFN$_{O-MMT}$ membrane at varying weight ratio of O-MMT and TMC. Feed = 1000 ppm Na$_2$SO$_4$ solution; Operating condition: pH = 7, 6 bar, 30 °C.
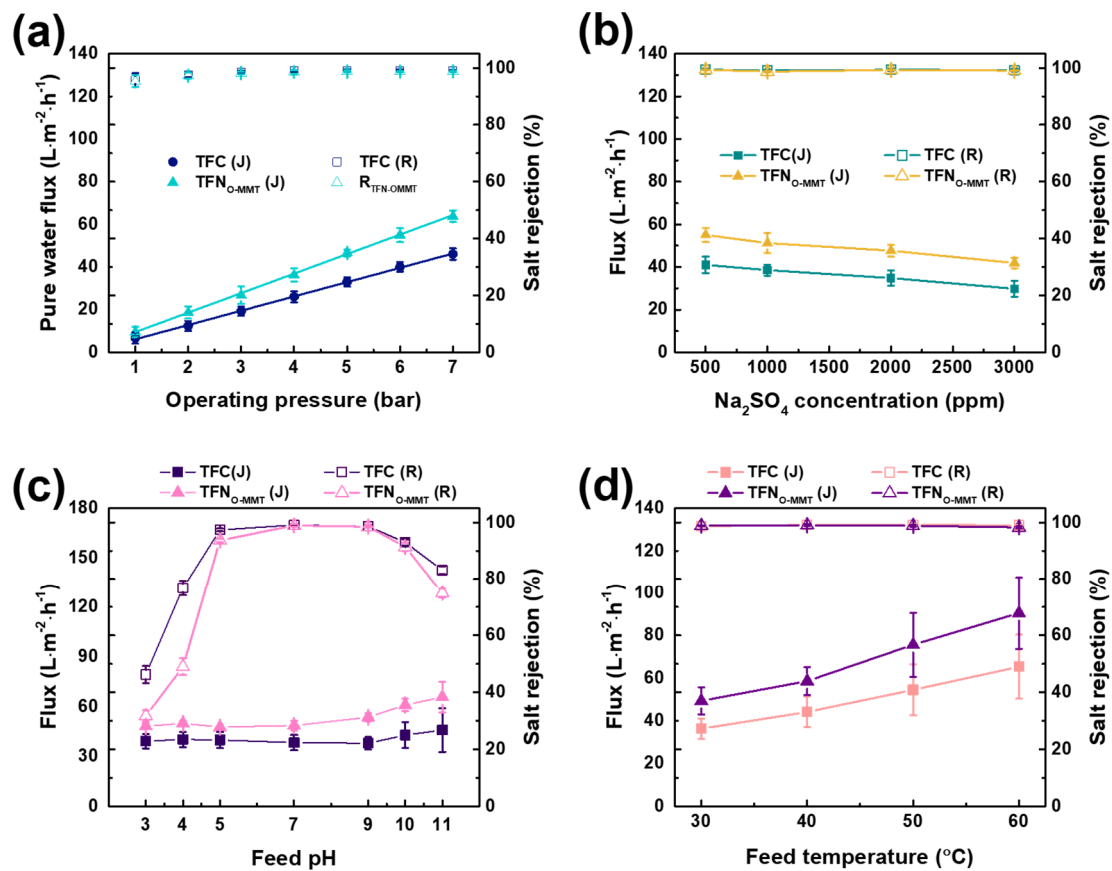
3.4. Operating Conditions

The testing conditions were varied to determine if the TFN$_{O-MMT}$ is stable at a wide range operation. Figure 12a reports the performance of TFC and TFN$_{O-MMT}$ membranes at different operating pressures from 1 to 7 bar. Both membranes displayed a linear increase in pure water flux. From 1 to 7 bar, pure water flux of TFC membrane increased from 6.71 ± 2.62 to 46.09 ± 2.70 L·m^{-2}·h^{-1}, whereas the flux of TFN$_{O-MMT}$ rose from 9.45 ± 2.49 to 63.75 ± 2.69 L·m^{-2}·h^{-1}. Both membranes maintained the salt rejection up to 99%. These results showed that TFN$_{O-MMT}$ still exhibited an advantage at a higher pressure, up to 7 bar.

The concentration of Na$_2$SO$_4$ in the feed varied from 500 to 3000 ppm (Figure 12b). At an increasing Na$_2$SO$_4$ concentration, the water flux of TFC and TFN$_{O-MMT}$ decreased from 41.00 ± 3.79 to 29.81 ± 3.67, and 55.06 ± 3.17 to 41.86 ± 2.54 L·m^{-2}·h^{-1}, respectively. The decrease of flux was attributed to the high osmotic pressure at high salt concentration, causing a decrease in the driving force to push the water to the other side of the membrane [82]. Furthermore, with a high salt concentration, the salts gathered on the membrane surface and a phenomenon called concentration polarization occurred. This event gives another mass transfer resistance that prevents the water from passing through the membrane [83]. Nonetheless, the salt rejection of the TFC and TFN$_{O-MMT}$ membrane was maintained at 99%. This shows that TFN$_{O-MMT}$ membrane could also operate at a wide salt concentration.

The feed pH affects the surface charge of the membrane; hence, it is important to determine the performance of the membrane from pH 3 to 11 (Figure 12c). Increasing the pH from 3 to 5, the Na$_2$SO$_4$ rejection of TFC and TFN$_{O-MMT}$ membranes was boosted from 46.24 ± 2.98 to 97.38 ± 0.48, and 31.74 ± 2.05 to 93.69 ± 0.64%, respectively. TFC and TFN$_{O-MMT}$ had low rejection at pH below 5. At low pH, the amine groups of TFC and TFN$_{O-MMT}$ membranes would protonate and give a more positively charged surface. This results in a higher chance of the SO$_3$$^{2-}$ being attracted to the membrane, leading to a higher chance of passing through the membrane. At pH 5 to 10, the salt rejection of the membrane was maintained at approximately 92% to 99%. At this pH, both membranes had a negatively charged surface because of deprotonation of the carboxyl groups and aluminosilicate groups in polyamide and O-MMT, respectively. According to Donnan exclusion, a negatively charged surface repels the anions (SO$_3$$^{2-}$) in a feed, resulting in high salt rejection. However, at pH 11, polyamide layer of TFC and TFN$_{O-MMT}$ was already swelled because most of the carboxyl groups or metal oxides were deprotonated—a repulsion among them and creating larger free volume in the polyamide chain. Hence,

the salt rejection of TFC and TFN$_{O-MMT}$ at pH 11 declined to 83.18 ± 1.37 and 74.93 ± 1.55%, respectively. This displays the importance of the feed pH in achieving the optimum operating condition.


Figure 12. Nanofiltration performance of TFC and TFN$_{O-MMT}$ at different operating conditions: (**a**) operating pressure; (**b**) Na$_2$SO$_4$ concentration; (**c**) feed pH; (**d**) feed temperature. Particle concentration = 0.05 g O-MMT/g TMC.

Figure 12d depicts the effect of feed temperature (30–60 °C) on the NF performance. TFC and TFN$_{O-MMT}$ membranes had a stable salt rejection at low and high operating temperatures, which was approximately 99.00%. TFN$_{O-MMT}$ had a higher flux than that of the TFC membrane for all range of temperature. With the increase of operating temperature from 30 to 60 °C, the flux of TFN$_{O-MMT}$ increased from 49.36 ± 6.35 to 90.50 ± 16.83 L·m^{-2}·h^{-1}, whereas the flux of TFC also increased from 36.32 ± 4.73 to 65.32 ± 15.00 L·m^{-2}·h^{-1}. At a high temperature, the mobility of water moves faster in comparison to a low temperature, thereby enhancing the water flux. The results indicated that TFN$_{O-MMT}$ was more advantageous than TFC membrane at a wide operating temperature.

3.5. Antifouling Property and Stability of the Membranes

The antifouling property of the membranes should be improved to increase their lifespan. Figure 13 demonstrates the antifouling behavior of TFC and TFN$_{O-MMT}$. The model foulant used was BSA. The fouling test was conducted for 3 cycles with the pH maintained at 7.4 using a phosphate-buffer saline solution. Similar to other works [84,85], reporting the normalized flux describes the antifouling capability of the membranes. For the first two cycles, the TFN$_{O-MMT}$ membrane had a similar normalized flux when the feed was either pure water or BSA+Na$_2$SO$_4$ solution. After three cycles, the normalized flux of the TFN$_{O-MMT}$ membrane increased to 1.34, whereas the TFC membrane had a normalized flux of 1.20. These results indicated that the TFN$_{O-MMT}$ membrane had a better antifouling property. Other works [86,87] reported that when BSA containing phosphate buffers saline in contact

with the membranes, it enlarged the membrane pores, resulting in an increase in flux. Figure 14 describes the stability of the TFC and TFN$_{O-MMT}$. It was evident that the membrane remained stable for 168-h, even after O-MMT modified the polyamide layer. Therefore, the membrane was stable for long term use.
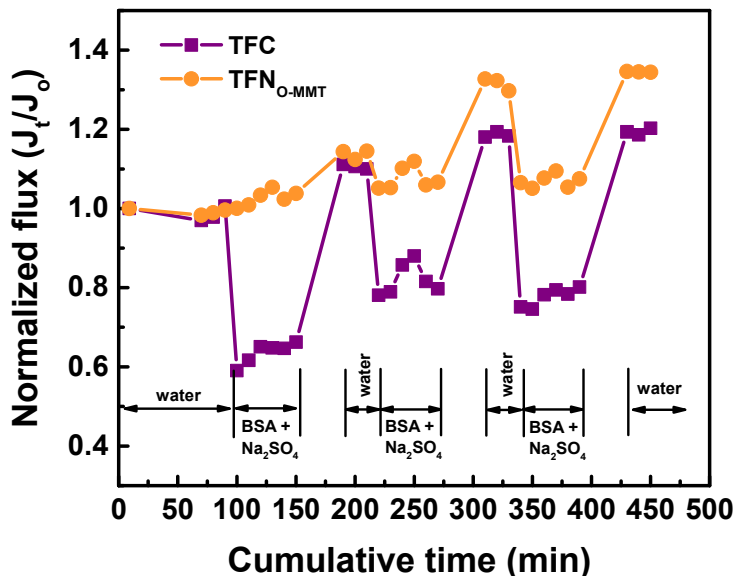
Figure 13. Antifouling property of TFC and TFN$_{O-MMT}$. Feed = 100 ppm BSA + 1000 ppm Na$_2$SO$_4$; Operating condition: pH = 7.4, 6 bar, 30 °C. The normalized flux was calculated as the ratio of flux (J$_t$) at time t over the initial flux (J$_o$) measurement.
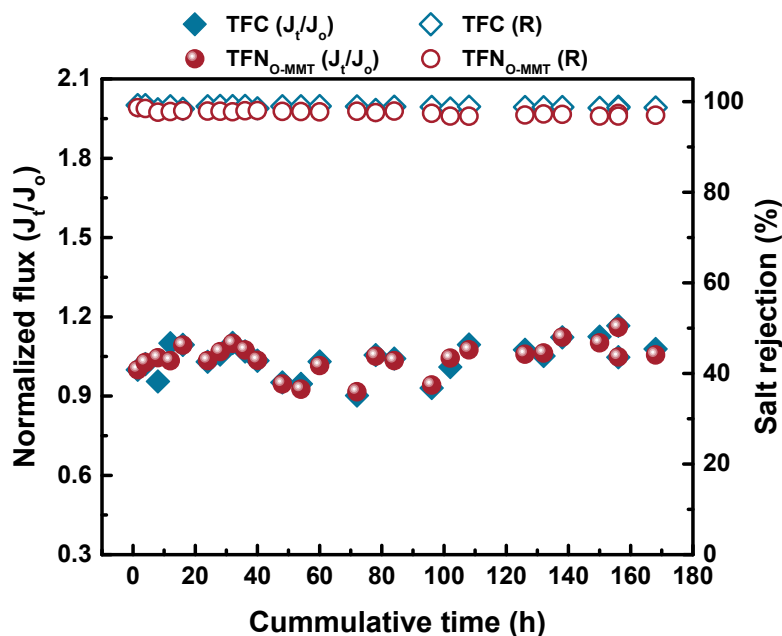
Figure 14. Stability test of TFC and TFN$_{O-MMT}$ membrane for 168-h. Feed = 1000 ppm Na2SO4 solution; Operating condition: pH = 7, 6 bar, 30 °C. The normalized flux was calculated as the ratio of flux (J$_t$) at time t over the initial flux (J$_o$) measurement.

4. Conclusions

The behavior of the nanoparticles in dispersion medium is critical to obtain a high membrane performance. The two types of MMT behaved differently when dispersed to n-hexane in TMC solution.

Intercalating DDA$^+$ in MMT produced a better dispersed MMT in n-hexane than intercalating Na$^+$. The surface of both MMTs became rough, resulting in an improvement in water flux and hydrophilicity. The TFN$_{O-MMT}$ had a more uniform surface than TFN$_{Na-MMT}$, because of the exfoliation of O-MMT in the n-hexane solution. The TFN$_{O-MMT}$ also had a more hydrophilic surface in comparison to other membranes, because the O-MMT was more hydrophilic than that of Na-MMT. Compared to pristine and TFN$_{Na-MMT}$, TFN$_{O-MMT}$ delivered the highest NF performance at its optimum concentration. TFN$_{O-MMT}$ was also stable on a wide operating condition and was suitable for long term use. Furthermore, the process of embedding O-MMT enhanced the antifouling property of the polyamide membrane.

Supplementary Materials: The following are available online at http://www.mdpi.com/2077-0375/10/5/79/s1, Figure S1: Dispersion of Na-MMT and O-MMT in n-hexane, Table S1: Surface area, total pore volume and pore size of MMTs.

References

1. Cheremisinoff, P.N. *Handbook of Water and Wastewater Treatment Technology*; Routledge: Abingdon, UK, 2018.
2. Bratby, J. *Coagulation and Flocculation in Water and Wastewater Treatment*; IWA Publishing: London, UK, 2016.
3. Baker, R.; Cussler, E.; Eykamp, W.; Koros, W.; Riley, R.; Strathmann, H. *Membrane Separation Systems-Recent Developments and Future Directions*; William Andrew Inc.: Westwood, NJ, USA, 1991.
4. Gin, D.L.; Noble, R.D. Chemistry. Designing the next generation of chemical separation membranes. *Science* **2011**, *332*, 674–676. [CrossRef] [PubMed]
5. Al-Najar, B.; Peters, C.D.; Albuflasa, H.; Hankins, N.P. Pressure and osmotically driven membrane processes: A review of the benefits and production of nano-enhanced membranes for desalination. *Desalination* **2020**, *479*, 114323. [CrossRef]
6. Van Der Bruggen, B.; Vandecasteele, C.; Van Gestel, T.; Doyen, W.; Leysen, R. A review of pressure-driven membrane processes in wastewater treatment and drinking water production. *Environ. Prog.* **2003**, *22*, 46–56. [CrossRef]
7. Vourch, M.; Balannec, B.; Chaufer, B.; Dorange, G. Nanofiltration and reverse osmosis of model process waters fromthe dairy industry to produce water for reuse. *Desalination* **2005**, *172*, 245–256. [CrossRef]
8. Zhou, D.; Zhu, L.; Fu, Y.; Zhu, M.; Xue, L. Development of lower cost seawater desalination processes using nanofiltration technologies—A review. *Desalination* **2015**, *376*, 109–116. [CrossRef]
9. Diawara, C.K. Nanofiltration process efficiency in water desalination. *Sep. Purif. Rev.* **2008**, *37*, 302–324. [CrossRef]
10. Salehi, F. Current and future applications for nanofiltration technology in the food processing. *Food Bioprod. Process.* **2014**, *92*, 161–177. [CrossRef]
11. Warczok, J.; Ferrando, M.; Lopez, F.; Güell, C. Concentration of apple and pear juices by nanofiltration at low pressures. *J. Food Eng.* **2004**, *63*, 63–70. [CrossRef]
12. Wu, M.; Sun, D.D. Characterization and reduction of membrane fouling during nanofiltration of semiconductor indium phosphide (inp) wastewater. *J. Membr. Sci.* **2005**, *259*, 135–144. [CrossRef]
13. Wu, M. Effect of operating variables on rejection of indium using nanofiltration membranes. *J. Membr. Sci.* **2004**, *240*, 105–111. [CrossRef]

14. Shams Ashaghi, K.; Ebrahimi, M.; Czermak, P.J.O.E.S. Ceramic ultra-and nanofiltration membranes for oilfield produced water treatment: A mini review. *Open Environ. Sci.* **2007**, *1*, 1–8. [CrossRef]

15. Nair, R.R.; Protasova, E.; Bilstad, T.; Strand, S. Evaluation of nanofiltration membrane process for smartwater production in carbonate reservoirs from deoiled produced water and seawater. *SPE Prod. Oper.* **2019**, *34*, 409–420. [CrossRef]

16. Foureaux, A.F.S.; Reis, E.O.; Lebron, Y.; Moreira, V.; Santos, L.V.; Amaral, M.S.; Lange, L.C. Rejection of pharmaceutical compounds from surface water by nanofiltration and reverse osmosis. *Sep. Purif. Technol.* **2019**, *212*, 171–179. [CrossRef]

17. Licona, K.P.M.; Geaquinto, L.R.d.O.; Nicolini, J.V.; Figueiredo, N.G.; Chiapetta, S.C.; Habert, A.C.; Yokoyama, L. Assessing potential of nanofiltration and reverse osmosis for removal of toxic pharmaceuticals from water. *J. Water Process Eng.* **2018**, *25*, 195–204. [CrossRef]

18. Lau, W.-J.; Ismail, A.F. Polymeric nanofiltration membranes for textile dye wastewater treatment: Preparation, performance evaluation, transport modelling, and fouling control—A review. *Desalination* **2009**, *245*, 321–348. [CrossRef]

19. Han, G.; Chung, T.S.; Weber, M.; Maletzko, C. Low-pressure nanofiltration hollow fiber membranes for effective fractionation of dyes and inorganic salts in textile wastewater. *Environ. Sci. Technol.* **2018**, *52*, 3676–3684. [CrossRef]

20. Paul, M.; Jons, S.D. Chemistry and fabrication of polymeric nanofiltration membranes: A review. *Polymer* **2016**, *103*, 417–456. [CrossRef]

21. Tul Muntha, S.; Kausar, A.; Siddiq, M. Advances in polymeric nanofiltration membrane: A review. *Polym. Plast. Technol. Eng.* **2016**, *56*, 841–856. [CrossRef]

22. Gohil, J.M.; Ray, P. A review on semi-aromatic polyamide tfc membranes prepared by interfacial polymerization: Potential for water treatment and desalination. *Sep. Purif. Technol.* **2017**, *181*, 159–182. [CrossRef]

23. Ehsan Yakavalangi, M.; Rimaz, S.; Vatanpour, V. Effect of surface properties of polysulfone support on the performance of thin film composite polyamide reverse osmosis membranes. *J. Appl. Polym. Sci.* **2017**, *134*. [CrossRef]

24. Ghosh, A.K.; Hoek, E.M.V. Impacts of support membrane structure and chemistry on polyamide–polysulfone interfacial composite membranes. *J. Membr. Sci.* **2009**, *336*, 140–148. [CrossRef]

25. Li, W.; Bian, C.; Fu, C.; Zhou, A.; Shi, C.; Zhang, J. A poly(amide-co-ester) nanofiltration membrane using monomers of glucose and trimesoyl chloride. *J. Membr. Sci.* **2016**, *504*, 185–195. [CrossRef]

26. Zuo, J.; Chung, T.-S. Design and synthesis of a fluoro-silane amine monomer for novel thin film composite membranes to dehydrate ethanol via pervaporation. *J. Mater. Chem. A* **2013**, *1*, 9814–9826. [CrossRef]

27. Tang, Y.-J.; Xu, Z.-L.; Xue, S.-M.; Wei, Y.-M.; Yang, H. A chlorine-tolerant nanofiltration membrane prepared by the mixed diamine monomers of pip and bhttm. *J. Membr. Sci.* **2016**, *498*, 374–384. [CrossRef]

28. An, Q.-F.; Sun, W.-D.; Zhao, Q.; Ji, Y.-L.; Gao, C.-J. Study on a novel nanofiltration membrane prepared by interfacial polymerization with zwitterionic amine monomers. *J. Membr. Sci.* **2013**, *431*, 171–179. [CrossRef]

29. De Guzman, M.R.; Ang, M.B.M.Y.; Lai, C.-L.; Trilles, C.A.; Pereira, J.M.; Aquino, R.R.; Huang, S.-H.; Lee, K.-R. Choice of apposite dispersing medium for silica nanoparticles leading to their effective embedment in nanocomposite nanofiltration membranes. *Ind. Eng. Chem. Res.* **2019**, *58*, 17937–17944. [CrossRef]

30. Kotlhao, K.; Lawal, I.A.; Moutloali, R.M.; Klink, M.J. Antifouling properties of silver-zinc oxide polyamide thin film composite membrane and rejection of 2-chlorophenol and 2,4-dichlorophenol. *Membranes* **2019**, *9*, 96. [CrossRef]

31. Yin, J.; Kim, E.-S.; Yang, J.; Deng, B. Fabrication of a novel thin-film nanocomposite (tfn) membrane containing mcm-41 silica nanoparticles (nps) for water purification. *J. Membr. Sci.* **2012**, *423–424*, 238–246. [CrossRef]

32. Liu, S.; Fang, F.; Wu, J.; Zhang, K. The anti-biofouling properties of thin-film composite nanofiltration membranes grafted with biogenic silver nanoparticles. *Desalination* **2015**, *375*, 121–128. [CrossRef]

33. Bano, S.; Mahmood, A.; Kim, S.-J.; Lee, K.-H. Graphene oxide modified polyamide nanofiltration membrane with improved flux and antifouling properties. *J. Mater. Chem. A* **2015**, *3*, 2065–2071. [CrossRef]

34. Yin, J.; Zhu, G.; Deng, B. Graphene oxide (go) enhanced polyamide (pa) thin-film nanocomposite (tfn) membrane for water purification. *Desalination* **2016**, *379*, 93–101. [CrossRef]

35. Lind, M.L.; Ghosh, A.K.; Jawor, A.; Huang, X.; Hou, W.; Yang, Y.; Hoek, E.M. Influence of zeolite crystal size on zeolite-polyamide thin film nanocomposite membranes. *Langmuir* **2009**, *25*, 10139–10145. [CrossRef] [PubMed]

36. Xiao, F.; Wang, B.; Hu, X.; Nair, S.; Chen, Y. Thin film nanocomposite membrane containing zeolitic imidazolate framework-8 via interfacial polymerization for highly permeable nanofiltration. *J. Taiwan Inst. Chem. Eng.* **2017**, *83*, 159–167. [CrossRef]

37. Li, N.; Yu, L.; Xiao, Z.; Jiang, C.; Gao, B.; Wang, Z. Biofouling mitigation effect of thin film nanocomposite membranes immobilized with laponite mediated metal ions. *Desalination* **2020**, *473*, 114162. [CrossRef]

38. Zhao, Q.; Zhao, D.L.; Chung, T.S. Nanoclays-incorporated thin-film nanocomposite membranes for reverse osmosis desalination. *Adv. Mater. Interfaces* **2020**, *7*, 1902108. [CrossRef]

39. Kadhom, M.; Deng, B. Thin film nanocomposite membranes filled with bentonite nanoparticles for brackish water desalination: A novel water uptake concept. *Microporous Mesoporous Mater.* **2019**, *279*, 82–91. [CrossRef]

40. Maalige, N.R.; Aruchamy, K.; Mahto, A.; Sharma, V.; Deepika, D.; Mondal, D.; Nataraj, S.K. Low operating pressure nanofiltration membrane with functionalized natural nanoclay as antifouling and flux promoting agent. *Chem. Eng. J.* **2019**, *358*, 821–830. [CrossRef]

41. Tajuddin, M.H.; Yusof, N.; Wan Azelee, I.; Wan Salleh, W.N.; Ismail, A.F.; Jaafar, J.; Aziz, F.; Nagai, K.; Razali, N.F. Development of copper-aluminum layered double hydroxide in thin film nanocomposite nanofiltration membrane for water purification process. *Front. Chem.* **2019**, *7*, 3. [CrossRef]

42. Tajuddin, M.H.; Yusof, N.; Abdullah, N.; Abidin, M.N.Z.; Salleh, W.N.W.; Ismail, A.F.; Matsuura, T.; Hairom, N.H.H.; Misdan, N. Incorporation of layered double hydroxide nanofillers in polyamide nanofiltration membrane for high performance of salts rejections. *J. Taiwan Inst. Chem. Eng.* **2019**, *97*, 1–11. [CrossRef]

43. Dong, H.; Wu, L.; Zhang, L.; Chen, H.; Gao, C. Clay nanosheets as charged filler materials for high-performance and fouling-resistant thin film nanocomposite membranes. *J. Membr. Sci.* **2015**, *494*, 92–103. [CrossRef]

44. Fathizadeh, M.; Tien, H.N.; Khivantsev, K.; Song, Z.; Zhou, F.; Yu, M. Polyamide/nitrogen-doped graphene oxide quantum dots (n-goqd) thin film nanocomposite reverse osmosis membranes for high flux desalination. *Desalination* **2019**, *451*, 125–132. [CrossRef]

45. Sun, H.; Wu, P. Tuning the functional groups of carbon quantum dots in thin film nanocomposite membranes for nanofiltration. *J. Membr. Sci.* **2018**, *564*, 394–403. [CrossRef]

46. Kim, E.-S.; Hwang, G.; Gamal El-Din, M.; Liu, Y. Development of nanosilver and multi-walled carbon nanotubes thin-film nanocomposite membrane for enhanced water treatment. *J. Membr. Sci.* **2012**, *394–395*, 37–48. [CrossRef]

47. Zarrabi, H.; Yekavalangi, M.E.; Vatanpour, V.; Shockravi, A.; Safarpour, M. Improvement in desalination performance of thin film nanocomposite nanofiltration membrane using amine-functionalized multiwalled carbon nanotube. *Desalination* **2016**, *394*, 83–90. [CrossRef]

48. Lau, W.J.; Gray, S.; Matsuura, T.; Emadzadeh, D.; Chen, J.P.; Ismail, A.F. A review on polyamide thin film nanocomposite (tfn) membranes: History, applications, challenges and approaches. *Water Res.* **2015**, *80*, 306–324. [CrossRef] [PubMed]

49. Jeong, B.-H.; Hoek, E.M.V.; Yan, Y.; Subramani, A.; Huang, X.; Hurwitz, G.; Ghosh, A.K.; Jawor, A. Interfacial polymerization of thin film nanocomposites: A new concept for reverse osmosis membranes. *J. Membr. Sci.* **2007**, *294*, 1–7. [CrossRef]

50. Buruga, K.; Song, H.; Shang, J.; Bolan, N.; Jagannathan, T.K.; Kim, K.H. A review on functional polymer-clay based nanocomposite membranes for treatment of water. *J. Hazard. Mater.* **2019**, *379*, 120584. [CrossRef]

51. Sanyal, O.; Liu, Z.; Yu, J.; Meharg, B.M.; Hong, J.S.; Liao, W.; Lee, I. Designing fouling-resistant clay-embedded polyelectrolyte multilayer membranes for wastewater effluent treatment. *J. Membr. Sci.* **2016**, *512*, 21–28. [CrossRef]

52. Dlamini, D.S.; Li, J.; Mamba, B.B. Critical review of montmorillonite/polymer mixed-matrix filtration membranes: Possibilities and challenges. *Appl. Clay Sci.* **2019**, *168*, 21–30. [CrossRef]

53. Uddin, F. Clays, nanoclays, and montmorillonite minerals. *Metall. Mater. Trans. A* **2008**, *39*, 2804–2814. [CrossRef]

54. 231, E.H.C. Bentonite, Kaloline, and Selected clay Minerals. Available online: www.inchem.org (accessed on 20 March 2020).

55. Brigatti, M.F.; Galan, E.; Theng, B. Structures and mineralogy of clay minerals. *Dev. Clay Sci.* **2006**, *1*, 19–86.

56. Basilia, B.A.; Mendoza, H.D.; Cada, L.G. Synthesis and characterization of rpet/organomontmorillonite nanocomposites. *Philipp. Eng. J.* **2002**, *23*, 19–34.

57. Inglethorpe, S.; Morgan, D.; Highley, D.; Bloodworth, J. Industrial minerals laboratory manual. In *British Geological Survey Technical Report*; WG/93/20, Mineralogy and Petrology Series; Natural Environment Research Council: Nottingham, UK, 1993.

58. Favre, H.; Lagaly, G. Organo-bentonites with quaternary alkylammonium ions. *Clay Miner.* **1991**, *26*, 19–32. [CrossRef]

59. Ang, M.B.M.Y.; Trilles, C.A.; De Guzman, M.R.; Pereira, J.M.; Aquino, R.R.; Huang, S.-H.; Hu, C.-C.; Lee, K.-R.; Lai, J.-Y. Improved performance of thin-film nanocomposite nanofiltration membranes as induced by embedded polydopamine-coated silica nanoparticles. *Sep. Purif. Technol.* **2019**, *224*, 113–120. [CrossRef]

60. Zhuang, G.; Zhang, H.; Wu, H.; Zhang, Z.; Liao, L. Influence of the surfactants' nature on the structure and rheology of organo-montmorillonite in oil-based drilling fluids. *Appl. Clay Sci.* **2017**, *135*, 244–252. [CrossRef]

61. Yang, S.; Zhao, D.; Zhang, H.; Lu, S.; Chen, L.; Yu, X. Impact of environmental conditions on the sorption behavior of pb(ii) in na-bentonite suspensions. *J. Hazard. Mater.* **2010**, *183*, 632–640. [CrossRef] [PubMed]

62. Motawie, A.M.; Madany, M.M.; El-Dakrory, A.Z.; Osman, H.M.; Ismail, E.A.; Badr, M.M.; El-Komy, D.A.; Abulyazied, D.E. Physico-chemical characteristics of nano-organo bentonite prepared using different organo-modifiers. *Egypt. J. Pet.* **2014**, *23*, 331–338. [CrossRef]

63. Tan, X.L.; Hu, J.; Zhou, X.; Yu, S.M.; Wang, X.K. Characterization of lin'an montmorillonite and its application in the removal of ni2+ from aqueous solutions. *Radiochim. Acta* **2008**, *96*, 487–495. [CrossRef]

64. Atia, A. Adsorption of chromate and molybdate by cetylpyridinium bentonite. *Appl. Clay Sci.* **2008**, *41*, 73–84. [CrossRef]

65. Ahmad, M.B.; Gharayebi, Y.; Salit, M.S.; Hussein, M.Z.; Shameli, K. Comparison of in situ polymerization and solution-dispersion techniques in the preparation of polyimide/montmorillonite (mmt) nanocomposites. *Int. J. Mol. Sci.* **2011**, *12*, 6040–6050. [CrossRef] [PubMed]

66. Lagaly, G. Interaction of alkylamines with different types of layered compounds. *Solid State Ionics* **1986**, *22*, 43–51. [CrossRef]

67. Ltifi, I.; Ayari, F.; Chehimi, D.B.H.; Ayadi, M.T. Physicochemical characteristics of organophilic clays prepared using two organo-modifiers: Alkylammonium cation arrangement models. *Appl. Water Sci.* **2018**, *8*, 91. [CrossRef]

68. Brum, M.C.; Capitaneo, J.L.; Oliveira, J.F. Removal of hexavalent chromium from water by adsorption onto surfactant modified montmorillonite. *Miner. Eng.* **2010**, *23*, 270–272. [CrossRef]

69. Marras, S.I.; Tsimpliaraki, A.; Zuburtikudis, I.; Panayiotou, C. Thermal and colloidal behavior of amine-treated clays: The role of amphiphilic organic cation concentration. *J. Colloid Interface Sci.* **2007**, *315*, 520–527. [CrossRef]

70. Kwon, Y.; Leckie, J. Hypochlorite degradation of crosslinked polyamide membranesii. Changes in hydrogen bonding behavior and performance. *J. Membr. Sci.* **2006**, *282*, 456–464. [CrossRef]

71. Tang, C.Y.; Kwon, Y.-N.; Leckie, J.O. Effect of membrane chemistry and coating layer on physiochemical properties of thin film composite polyamide ro and nf membranes. *Desalination* **2009**, *242*, 149–167. [CrossRef]

72. Ang, M.B.M.Y.; Lau, V.J.; Ji, Y.L.; Huang, S.H.; An, Q.F.; Caparanga, A.R.; Tsai, H.A.; Hung, W.S.; Hu, C.C.; Lee, K.R.; et al. Correlating psf support physicochemical properties with the formation of piperazine-based polyamide and evaluating the resultant nanofiltration membrane performance. *Polymers* **2017**, *9*, 505. [CrossRef]

73. Xiang, J.; Xie, Z.; Hoang, M.; Zhang, K. Effect of amine salt surfactants on the performance of thin film composite poly(piperazine-amide) nanofiltration membranes. *Desalination* **2013**, *315*, 156–163. [CrossRef]

74. Li, L.; Zhang, S.; Zhang, X. Preparation and characterization of poly(piperazineamide) composite nanofiltration membrane by interfacial polymerization of 3,3',5,5'-biphenyl tetraacyl chloride and piperazine. *J. Membr. Sci.* **2009**, *335*, 133–139. [CrossRef]

75. Meihong, L.; Sanchuan, Y.; Yong, Z.; Congjie, G. Study on the thin-film composite nanofiltration membrane for the removal of sulfate from concentrated salt aqueous: Preparation and performance. *J. Membr. Sci.* **2008**, *310*, 289–295. [CrossRef]

76. BA, F.; AE, Y. Removal of cationic dye (basic red 18) from aqueous solution using natural turkish clay. *Glob. Nest J.* **2013**, *15*, 529–541.

77. Liu, H.; Zhang, M.; Zhao, H.; Jiang, Y.; Liu, G.; Gao, J. Enhanced dispersibility of metal–organic frameworks (mofs) in the organic phase via surface modification for tfn nanofiltration membrane preparation. *RSC Adv.* **2020**, *10*, 4045–4057. [CrossRef]

78. Yang, S.; Zhang, K. Few-layers mos2 nanosheets modified thin film composite nanofiltration membranes with improved separation performance. *J. Membr. Sci.* **2020**, *595*, 117526. [CrossRef]

79. Hu, J.; Lv, Z.; Xu, Y.; Zhang, X.; Wang, L. Fabrication of a high-flux sulfonated polyamide nanofiltration membrane: Experimental and dissipative particle dynamics studies. *J. Membr. Sci.* **2016**, *505*, 119–129. [CrossRef]

80. Nightingale, E.R. Phenomenological theory of ion solvation. Effective radii of hydrated ions. *J. Phys. Chem.* **1959**, *63*, 1381–1387. [CrossRef]

81. Yaroshchuk, A. Non-steric mechanisms of nanofiltration: Superposition of donnan and dielectric exclusion. *Sep. Purif. Technol.* **2001**, *22–23*, 143–158. [CrossRef]

82. Spiegler, K.S.; Kedem, O. Thermodynamics of hyperfiltration (reverse osmosis): Criteria for efficient membranes. *Desalination* **1966**, *1*, 311–326. [CrossRef]

83. García-Martín, N.; Silva, V.; Carmona, F.J.; Palacio, L.; Hernández, A.; Prádanos, P. Pore size analysis from retention of neutral solutes through nanofiltration membranes. The contribution of concentration–polarization. *Desalination* **2014**, *344*, 1–11. [CrossRef]

84. Lu, P.; Liang, S.; Zhou, T.; Xue, T.; Mei, X.; Wang, Q. Layered double hydroxide nanoparticle modified forward osmosis membranes via polydopamine immobilization with significantly enhanced chlorine and fouling resistance. *Desalination* **2017**, *421*, 99–109. [CrossRef]

85. Lu, P.; Li, W.; Yang, S.; Liu, Y.; Wang, Q.; Li, Y. Layered double hydroxide-modified thin–film composite membranes with remarkably enhanced chlorine resistance and anti-fouling capacity. *Sep. Purif. Technol.* **2019**, *220*, 231–237. [CrossRef]

86. Ang, M.B.M.Y.; Ji, Y.L.; Huang, S.H.; Lee, K.R.; Lai, J.Y. A facile and versatile strategy for fabricating thin-film nanocomposite membranes with polydopamine-piperazine nanoparticles generated in situ. *J. Membr. Sci.* **2019**, *579*, 79–89. [CrossRef]

87. Shen, L.; Feng, S.; Li, J.; Chen, J.; Li, F.; Lin, H.; Yu, G. Surface modification of polyvinylidene fluoride (pvdf) membrane via radiation grafting: Novel mechanisms underlying the interesting enhanced membrane performance. *Sci. Rep.* **2017**, *7*, 1–13. [CrossRef] [PubMed]